

TWO-DIMENSIONAL MODELING AND ANALYSIS OF THIN
ELECTROELASTIC STRUCTURES WITH APPLICATION TO ACTUATOR AND
SENSOR DEVICE DESIGN

YADWINDER SINGH JOSHAN



DEPARTMENT OF APPLIED MECHANICS
INDIAN INSTITUTE OF TECHNOLOGY DELHI

MARCH 2023

© Indian Institute of Technology Delhi (IITD), New Delhi, 2023

**Two-dimensional Modeling and Analysis of Thin
Electroelastic Structures with Application to Actuator and
Sensor Device Design**

by

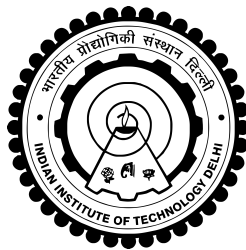
YADWINDER SINGH JOSHAN

DEPARTMENT OF APPLIED MECHANICS

Submitted

in fulfilment of requirements for the degree of Doctor of Philosophy

to the



INDIAN INSTITUTE OF TECHNOLOGY DELHI

MARCH 2023

Certificate

This is to certify that the thesis entitled, **‘Two-dimensional Modeling and Analysis of Thin Electroelastic Structures with Application to Actuator and Sensor Device Design’** submitted by **Mr. Yadwinder Singh Joshan** to the **Indian Institute of Technology Delhi** for the award of degree of **Doctor of Philosophy** embodies original research work done by him under my supervision. In my opinion, the thesis work meets the requisite standards and the candidate is worthy of consideration for the degree of Doctor of Philosophy in accordance with the regulations of the institute. The contents of this thesis have not been submitted to any other University or Institute for the award of any degree or diploma.

Place: New Delhi, India

Dr. Sushma Santapuri

Associate Professor

Department of Applied Mechanics

Indian Institute of Technology Delhi

Acknowledgments

First and foremost, I would like to express my sincere gratitude to my supervisor who guided me through this difficult journey from an inexperienced student to an independent researcher. Prof. Sushma Santapuri is more like a friend and a mentor to me than a supervisor. I always felt comfortable working with her because she calmly listened to all the problems I faced related to my research work and suggested immediate solutions. She not only helped me with her experienced opinions on my area of research but also helped me in improving my writing skills so that I could effectively communicate the idea and findings in research publications. I also want to thank Prof. Arun Srinivasa, who has always motivated me during my research journey and helped me broaden my horizon towards applied research.

I would also like to thank my SRC (student research committee) members, Prof. M. K. Singha, Prof. S. Pradyumna and Prof. S. P. Singh for their insightful comments and encouragement during the evaluation process of my doctoral work. I would also like to acknowledge Ministry of Human Resource and Development, Government of India for the financial assistance to carry out my doctoral research work at IIT Delhi.

My best friend Mohit Garg, who helped me maintain a positive frame of mind even in the depths of despair. My senior colleagues, Sandeep Singh, Gaurav Watts and Vishwanath Managuli, who mentored me during the initial but difficult phase of my PhD life. I would always cherish the conversations I had over a cup of tea with my friends Mohit, Adnan, Bishweshwar, Bhaba, Gargi, Anurag, Mehnaz, Amit, Sajjan, Raushan, Sriram, Bashir, Hasan, Ankita, Kuldeep, Anoop, Kamal, Gaurav, Ranjeet, and my junior colleagues, Rishab, Sumit, Mayank, Awantika, Intaf, Ayush, Satyendra, Saurabh, Nikesh,

Rishi, Devansh, Vikram and Aquib. Computational Lab has now become an extended family to me away from my home.

I have no words to express my gratitude to my parents, who provided immense emotional support which kept me motivated to complete my work. I hope I can repay the trust they showed in me by supporting them for the rest of my life. I wish to make them prouder by becoming better human beings and by contributing to society as a researcher.

Yadwinder Singh Joshan

Abstract

In this work, two-dimensional asymptotic theories are presented for modeling and analysis of electroelastic structures in different operational regimes with application to design of actuator and sensor devices. Three types of electroelastic materials, namely, piezoelectric materials, flexoelectric materials and dielectric elastomers are analyzed for different transducer applications. The two-dimensional models are developed specifically for each material based on the type of electromechanical coupling and requirements of the application.

Piezoelectric materials are explored for the design of torsional and transverse shear sensors using a novel non-polynomial electromechanical shell theory. The 2D shell theory is utilized to analyze piezoelectric shear sensors made of low symmetry materials with simple patch geometries in different operating modes. The electric potential and displacement fields are assumed to be inverse-hyperbolic functions of the thickness coordinate. A new computationally efficient C^0 continuous deep shell finite element framework is developed starting from the principle of minimum potential energy and additional continuity requirements are imposed through the use of penalty parameter approach. The results are verified by comparing with 3D FEM results. It is also observed that the inverse-hyperbolic theory has higher accuracy compared to the third-order polynomial theory for same number of degrees of freedom. Parametric studies are subsequently performed to analyze the effect of geometric parameters and loading conditions on the sensor response of piezoelectric shell structures.

Flexoelectric materials are analyzed using a novel gradient electromechanical theory that incorporates both direct and converse flexoelectric effects. The two-way coupled

electromechanical theory is developed starting from a 3D variational formulation by considering an electric field-strain based free energy function. The formulation incorporates mechanical as well as electrical size effects. This theory is used to analyze flexoelectric beams and plates in actuator and sensor modes. A novel C^2 continuous finite element framework is developed to solve the beam and plate governing equations. Our finite element results are verified with analytical solutions for simply-supported boundary conditions. The computational framework is subsequently used to perform various parametric studies to analyze the effect of electrical and mechanical length scale parameters and geometric parameters on the response of the flexoelectric structures. Our simulation results also agree well with the trends observed in recent experiments.

Finally, dielectric elastomers are analyzed for the design of soft membrane actuators. The membrane actuators are modelled using an $O(h)$ non-linear membrane theory incorporating finite deformations. Specifically, the deformations in circular and cylindrical membrane actuators are analyzed under applied pressure and electric field. The limit point instability in electroelastic membranes due to applied loads is also investigated as these instabilities can lead to failure in dielectric elastomer actuators due to dielectric breakdown.

In summary, two-dimensional frameworks applicable for the computational design and analysis of dielectric electroelastic materials based actuators and sensors are developed in this work. The utility of these models is demonstrated by applying it to different devices based on the regime of operation.

सारांश

इस कार्य में वैद्युत प्रत्यास्थित ढांचे के प्रतिरूपन और विश्लेषण के विभिन्न संचालन व्यवस्था के अन्तर्गत प्रवर्तक और संवेदक उपकरणों के उपयोग के लिए द्वि-आयामी स्पर्शोन्मुख सिद्धांतों को प्रस्तुत किया गया है। दाब विद्युत प्रदार्थ, फ्लेक्सोइलेक्ट्रिक प्रदार्थ और परावैद्युत प्रत्यास्थित नामक तीन प्रकार के वैद्युत प्रत्यास्थित प्रदार्थों का विश्लेषण विभिन्न ट्रांसड्यूसर उपयोग के लिए किया गया है। विशेष रूप से विद्युतयांत्रिकी युग्मन और उपयोग के रूपरेखा पर आधारित प्रत्येक प्रदार्थ के लिए द्वि-आयामी नमूने विकसित किए गए हैं।

आधुनिक और अनुप्रस्थ अपरूपन संवेदक की अभिकल्पना एक नई गैर बहुपदीय विद्युत यांत्रिकी शैल सिद्धांत द्वारा की गई है जिसमें दाब विद्युत पदार्थों का अन्वेषण किया गया है। द्वि-आयामी शैल सिद्धांत का उपयोग लघु समरूपक पदार्थ से बने साधारण पैच ज्यामिति वाले दाब विद्युत अपरूपन संवेदक के विश्लेषण में विभिन्न परिचालन तरीके में किया गया है। विद्युत विभव और विस्थापन क्षेत्र को मोटाई निर्देशांक का विपरीत अतिपर्वलिक फलन माना गया है। न्यूनतम स्तिथिज ऊर्जा के सिद्धांत से शुरुआत करके एक नई कुशल गणनात्मक सी⁰ सतत दीप शैल परिमित घटकीय रूपरेखा विकसित की गई है जिसमें पेनल्टी पैरामीटर का इस्तेमाल करते हुए अतिरिक्त सतत आवश्यकताएं अधिरोपित की गई हैं। परिणामों का सत्यापन त्रि-आयामी परिमित घटक तरीके के परिणामों से तुलना करके किया गया है। यह भी देखा जाता है कि समान संख्या की स्वतंत्र कोटी के लिए विपरीत अतिपर्वलिक सिद्धांत त्रिकोटिए बहुपद सिद्धांत की तुलना में अधिक सटीकता रखता है। ज्यामितीय मापदंड और लदन अवस्थाओं का दाब विद्युत शैल ढांचे के संवेदकीय जवाब के प्रभाव का मापदंडिये विश्लेषण का अध्ययन किया गया है।

फ्लेक्सोइलेक्ट्रिक पदार्थों का विश्लेषण एक नवीनतम ग्रेडिएंट इलेक्ट्रो-मैकेनिकल सिद्धांत से किया गया है जिसमें दोनो अपरोक्ष और परोक्ष फ्लेक्सोइलेक्ट्रिक प्रभाव समिलित हैं। एक विधुतिए क्षेत्र विकृति आधारित मुक्त ऊर्जा फलन को मान कर एक त्रि-आयामी परिवर्तनशील सूत्रीकरण से शुरुआत करते हुए दो तरफ़ी जुड़े इलेक्ट्रो-मैकेनिकल सिद्धांत को विकसित किया गया है। यह सूत्रीकरण यांत्रिकी के साथ ही विद्युत आकार के प्रभाव शामिल करता है। यह सिद्धांत फ्लेक्सोइलेक्ट्रिक बीम और प्लेट का प्रवर्तक और संवेदक तरीके में विश्लेषण करती है।

बीम और प्लेट की नियामक समीकरणों को हल करने के लिए एक नवीनतम सी² सतत परिमित घटकिए रूपरेखा विकसित की गई है। सरल समर्थित सीमा शर्तों के लिए हमारे परिमित घटकिए परिणाम को विश्लेषणात्मक हल से सत्यापित किया गया है। तत्पश्चात विद्युत और यांत्रिकीय लाम्बिक मापदंड पैमानों और ज्यामिति मापदंडों के प्रभाव का अध्ययन फ्लेक्सोइलेक्ट्रिक ढांचे के जवाब पर विभिन्न मापदंडों के अंतर्गत गणनात्मक रूपरेखा का प्रयोग कार्ट³ हुए किया गया है। हमारे अनुकूलन परिणाम भी हाल के प्रयोग में देखे गए प्रवृत्तियों से अच्छी तरह से सहमत होते हैं।

अंतिम रूप में नरम परत प्रवर्तकों की रचना के लिए परावैद्युत प्रत्यास्थलक का विश्लेषण किया गया है। एक औ(एच) गैर रेखीय परत सिद्धांत में परिमित विरूपण लेते हुए परत प्रवर्तक का प्रारूप किया गया है। विशेष रूप से गोलाकार और बेलनकार परत प्रवर्तकों की विकृतियों का विश्लेषण प्रयुक्त दाब और विद्युत क्षेत्र के तहत किया गया है। प्रयुक्त बल के कारण विद्युत प्रत्यास्थ परतों की सीमा स्थिरता को

भी जांचा गया है क्योंकि परावैद्युत विकार के कारण यह अस्थिरता परावैद्युत प्रत्यास्थलक प्रवर्तक की असफलता के लिए ज़िम्मेदार हो सकती है।

सारांश में परावैद्युत विद्युत प्रत्यास्थ पदार्थ आधारित प्रवर्तक और संवेदक के संगणनीय रचना और विश्लेषण के लिए उपयोगी द्वि-आयामी ढांचे इस काम में विकसित किए गए हैं। इन मॉडलों की उपयोगिता संचालन व्यवस्था पर आधारित विभिन्न उपकरणों पर लागू करके दिखाई गई है।

Table of Contents

Certificate	iii
Acknowledgments	v
Abstract	vii
List of Figures	xiii
List of Tables	xix
List of Symbols	xxi
Acronyms	xxv
1 Introduction	1
2 Literature Review	7
2.1 Modeling of Piezoelectric Materials	7
2.2 Modeling of Flexoelectric Materials	12
2.3 Modeling of Dielectric Elastomers	16
2.4 Scope and Objectives	20
3 Modeling and Analysis of Low Symmetry Piezoelectric Plates and Shells for Design of Shear Sensors	22
3.1 Mathematical Formulation	22
3.1.1 Structural Kinematics	23
3.1.2 Principle of Minimum Potential Energy	31
3.2 Finite Element Framework	32
3.2.1 Penalty Parameter Approach	32
3.2.2 Matrix Representation	34
3.2.3 Shape Functions	36
3.2.4 2D Finite Element Formulation	38
3.3 Results and Discussion	42
3.3.1 Benchmark Mechanical Convergence Tests	45
3.3.2 Sensor Response of Piezoelectric Cylindrical Shells with Extension-Electric Field Coupling	49
3.3.3 Analysis of Piezoelectric Torsional Sensor Exhibiting In-Plane Shear-Electric Field Coupling	56
3.3.4 Analysis of Shear Sensor Exhibiting Transverse Shear-Electric Field Coupling	60

3.3.5	Comparative Analysis of the Flexural, In-plane and Transverse Shear Sensors	64
3.4	Summary	64
4	A Gradient Electromechanical Theory for Flexoelectric Beams and Plates with Application to Microscale Sensor and Actuator Devices	66
4.1	3D Governing Equations and Boundary Conditions	67
4.2	Linear Flexoelectric Constitutive Modeling	73
4.2.1	Specialization to Isotropic Materials	74
4.3	Modeling of Flexoelectric Composite Plates	78
4.3.1	Derivation of Plate Governing Equations	82
4.3.2	2D Finite Element Formulation of a Flexoelectric Composite Plate	90
4.3.3	Matrix Representation	96
4.3.4	Derivation of Finite Element Formulation	98
4.4	Modelling of Flexoelectric Curved Beams	101
4.4.1	Two-way Coupled Flexoelectric Beam Formulation	104
4.4.2	Finite Element Framework for Flexoelectric Curved Beams	109
4.4.3	Derivation of Finite Element Governing Equations	110
4.5	Results and Discussion	113
4.5.1	Analysis of Flexoelectric Composite Plates	113
4.5.2	Analysis of Flexoelectric Curved Composite Beams	129
4.5.3	Bending Analysis of a Passive Isotropic Micro-beam	131
4.5.4	Bending Analysis of Flexoelectric Curved Beams under Applied Mechanical Load: Sensor Mode	132
4.5.5	Bending Analysis of Flexoelectric Curved Beams under Applied Electrical Load: Actuator Mode	134
4.6	Summary	135
5	Modeling and Analysis of Soft Electroelastic Membranes	137
5.1	3D Governing Equations	137
5.2	Membrane Formulation	139
5.2.1	Variational Formulation	142
5.3	Cylindrical Membrane Formulation under Axisymmetric Loading	146
5.3.1	Principle Stretch-based Formulation	148
5.4	Circular Membrane Formulation	156
5.5	Results and Discussion	160
5.5.1	Analysis of Electroelastic Circular Membranes	161
5.5.2	Analysis of Electroelastic Cylindrical Membranes	164
5.6	Summary	169
6	Conclusion and Future Scope of the Work	170
6.1	Conclusions	170
6.1.1	Analysis of Piezoelectric Shell Structures with Application to Shear Sensing	171
6.1.2	Modeling and Analysis of Flexoelectric Beam and Plate Structures	172
6.1.3	Large Deformation Theory for Electroelastic Membrane Actuators	173
6.2	Future Scope of the Work	174
	References	175

Appendices	196
A	196
B	201
C	208
Publications from the Present Work	213
About the Author	214

List of Figures

Figure 1.1:	Movement of dipoles in piezoelectric materials due to applied electric field causing mechanical deformations.	2
Figure 1.2:	Polarization of a centro-symmetric flexoelectric crystal due to applied strain gradient.	3
Figure 1.3:	(a) Variation of the electric field in a trapezoid for an applied potential difference giving rise to electric field gradient. (b) Deformation in a trapezoid under an applied electric field gradient due to the converse flexoelectric effect (Fu <i>et al.</i> (2006)).	4
Figure 1.4:	Stretching in dielectric elastomers on application of external electric field.	5
Figure 2.1:	Limit point or snap-through instability in dielectric elastomer membranes due to applied voltage.	17
Figure 3.1:	A doubly curved shell of principal radii of curvature R_1 and R_2	23
Figure 3.2:	Variation of nondimensional transverse shear stress T_4 across the thickness of a four-layered [0/90/90/0] laminated plate ($a/h = 10$) under sinusoidal load ($q_3 = q_0 \sin(\pi\alpha_1/a) \sin(\pi\alpha_2/b)$) for simply supported boundary conditions. Transverse shear stress at inter-laminar surfaces ($\alpha_3/h = -0.25, 0.25$) is found to be continuous as shown in the 3D FEM results. However, IHSDT (present theory), HSDT and FSDT results predict discontinuous stress variation across the thickness (Reddy (1984c)).	27
Figure 3.3:	Variation of nondimensional deflection with shape parameter r for a four-layered [0/90/90/0] laminated cylindrical shell ($a/h = 10$) under uniform pressure and simply supported boundary conditions for the following a/R values: (a) $a/R = 0.5$ (shallow shell), and (b) $a/R = 1$ (deep shell). The optimized value of $r = 0.32$ is obtained by comparing with 3D FEM results for both the cases.	29
Figure 3.4:	Schematic of a Scordelis-Lo barrel vault under self weight. Only a quarter of the section is analyzed by applying symmetry conditions. The maximum deflection normalized by the factor 0.3024 (analytical solution) is calculated at the center of free edge. A 4×4 mesh of the shell elements is shown.	46
Figure 3.5:	Comparison of the normalized deflection obtained using various shell theories for the Scordelis-Lo barrel vault problem. IHSDT results converge for a mesh size of 8×8	47

Figure 3.6:	Boundary and loading conditions for pinched cylinder with end diaphragms. One-eighth of the cylinder is analyzed due to symmetry of the problem. A mesh of 4×4 elements is shown.	47
Figure 3.7:	Comparison of normalized deflection at the center of the section for a pinched cylinder under point loads, obtained using different shell formulations. Converged results are obtained for a mesh size of 32×32 .	48
Figure 3.8:	Schematic of a flexural load sensor made of a piezoelectric layer (PFRC) at the top and a passive composite substrate at the bottom. PFRC is a uniaxially symmetric piezoelectric material and exhibits the coupling of in-plane normal stress with electric field.	49
Figure 3.9:	Convergence study of the nondimensional potential $\bar{\Phi}(0.5a, 0.5b, 0.5h)$ for different mesh sizes. The results are obtained for a plate ($a/R = 0$) and a deep shell ($a/R = 1$) for different boundary conditions. Converged results are obtained for a mesh size of 18×18 in all the cases.	50
Figure 3.10:	Nondimensional potential $\bar{\Phi}(0.5a, 0.5b, 0.5h)$ generated at the center of the piezoelectric unimorph [0/PFRC] flexural sensor under uniform pressure for different combinations of simply supported and clamped edge boundary conditions ($a/h = 10$).	52
Figure 3.11:	Contour plots of nondimensional potential $\bar{\Phi}$ for piezoelectric unimorph [0/PFRC] flexural sensor under uniform pressure for SSSS and SCSC boundary conditions ($a/h = 10$). The maximum potential is obtained at the center of the plate in case of SSSS, and at the center of the clamped edges for SCSC. Compare with contour plots for the in-plane shear torsional sensor and transverse shear sensor presented in Figures 3.15 and 3.21 respectively.	53
Figure 3.12:	Variation of nondimensional potential $\bar{\Phi}$ along the curve ($\alpha_1 = 0.5a$, $\alpha_3 = 0.5h$), for piezoelectric unimorph [0/PFRC] cylindrical shell under uniform pressure for simply supported boundary conditions ($a/h = 10$). The point of maximum potential is highlighted by a cross symbol.	54
Figure 3.13:	Variation of electrostatic potential $\Phi(0.5a, 0.5b, 0.5h)$ with thickness of PFRC layer for piezoelectric unimorph [0/PFRC] shell sensor under uniform pressure and simply supported boundary conditions ($a/h = 20$). The maximum potential is obtained for thickness ratio in the range of 0.7 - 0.8.	55
Figure 3.14:	Geometry of the torsional shear sensor. The cylindrical patch sensor consists of a low symmetry piezoelectric material (Rochelle Salt) at the top and a composite substrate layer at the bottom. The sensor is subjected to uniform shear traction q_{2s}	57

Figure 3.15:	Contour plot of nondimensional potential $\hat{\Phi}$ for a piezoelectric unimorph plate [0/RS] ($a/h = 10$) under torsional/in-plane shear loading. Note that the maximum potential is observed along $\alpha_2 = 0.5b$ and the plot is symmetric about this line. Compare with contour plots for the flexural and transverse shear sensors presented in Figures 3.11 and 3.21, respectively.	58
Figure 3.16:	Nondimensional potential $\hat{\Phi}(0.5a, 0.5b, 0.5h)$ generated across the piezoelectric unimorph [0/RS] torsional sensor for different a/R and a/h values. Compare with the transverse shear sensor output in Figure 20.	59
Figure 3.17:	Variation of nondimensional potential $\hat{\Phi}$ along the curve ($\alpha_2 = 0.5b$, $\alpha_3 = 0.5h$), for piezoelectric unimorph [0/RS] cylindrical shell ($a/h = 10$). The electrostatic potential is maximum at $\alpha_1 = 0.69a$ for $a/R=0, 1, 2$ and for $a/R = 3.14$, the maximum potential is obtained at $\alpha_1 = 0.55a$	59
Figure 3.18:	Variation of electrostatic potential $\Phi(0.5a, 0.5b, 0.5h)$ with thickness of RS layer for piezoelectric unimorph [0/RS] torsional sensor ($a/h = 20$). The maximum potential is observed for $h_p = h$, i.e., no substrate.	60
Figure 3.19:	A schematic of transverse shear sensor made of three-layered piezoelectric composite shell. A layer of piezoelectric material having orthotropic symmetry (PZT) with poling direction along α_1 is placed at the core of smart composite shell. The change in the orientation of poling direction enables transverse shear-electric field coupling in the piezoelectric material.	61
Figure 3.20:	Nondimensional potential $\tilde{\Phi}(0, 0.5b, 0.5h_p)$ generated in piezoelectric transverse shear sensor [0/PZT/0] under uniform pressure for different boundary conditions: (a) effect of span-to-thickness ratio ($a/R = 0$), (b) effect of depth of the shell ($a/h = 10$). Compare with the output of torsional/in-plane shear sensor in Figure 16.	62
Figure 3.21:	Contour plots of nondimensional potential $\tilde{\Phi}$ generated in a three-layered piezoelectric transverse shear sensor [0/PZT/0] under uniform pressure for SCSS and SCSC boundary conditions ($a/h = 10$). The contour plots are observed to be anti-symmetric about $\alpha_1 = 0.5a$. Compare with contour plots for the flexural and torsional shear sensors presented in Figures 3.11 and 3.15, respectively.	63
Figure 3.22:	Variation in electrostatic potential $\Phi(0, 0.5b, 0.5h_p)$ with thickness of RS layer for piezoelectric torsional shell sensor [0/PZT/0] under uniform pressure for SCSC boundary conditions ($a/h = 10$). The maximum potential is obtained for thickness ratio h_p/h in the range of 0.7 - 0.9.	64
Figure 4.1:	Schematic of the flexoelectric composite plate. A flexoelectric layer of thickness h_f is considered at the the top of a passive substrate.	78

Figure 4.2:	A two-dimensional four noded rectangular element. α_1^e and α_2^e are two-dimensional coordinates of the element.	91
Figure 4.3:	Schematic of a laminated composite flexoelectric curved beam consisting of a flexoelectric layer at the top and a passive substrate layer at the bottom.	102
Figure 4.4:	Converge of nondimensional transverse deflection w/h of a passive simply-supported micro-plate for conforming and non-conforming elements. The present FEM results agree well with analytical results presented in Akgöz and Civalek (2015) ($h = 11.01 \mu\text{m}$, $a = b = 40h$, $l_0 = l_1 = l_2 = 11.01 \mu\text{m}$).	117
Figure 4.5:	Convergence of nondimensional potential $\bar{\Phi}(a/2, b/2, h/2)$ with mesh size for simply-supported boundary conditions. The computational time taken by non-conforming finite element is 12.18 seconds and conforming element takes 22.59 seconds for 16×16 mesh	119
Figure 4.6:	Contour plots of nondimensional potential $\bar{\Phi}$ of flexoelectric unimorph plate for various boundary conditions ($h = 2 \mu\text{m}$, $a = b = 100h$, UDL).	120
Figure 4.7:	Contribution of converse flexoelectric effect in the overall flexoelectric response in sensor mode. The converse flexoelectric effect gives rise to a larger effective flexoelectric response ($a = b$, $a = 100h$, $h_f/h = 0.5$).	121
Figure 4.8:	Effective piezoelectric coefficient d_{31} for different scales of thickness for a one edge clamped flexoelectric plate sensor ($a = b$, $a = 100h$, $h_f/h = 1$). The value of effective piezoelectric coefficient is higher for flexoelectric material than piezoelectric materials for $h \leq 8 \mu\text{m}$. Similar trend in the results is observed by Abdollahi <i>et al.</i> (2019) in their experimental studies.	122
Figure 4.9:	Effect of electrical length scale parameter ratio l/h on nondimensional potential $\bar{\Phi}$ of a cantilever flexoelectric plate. Increase in l/h ratio increases the higher-order permittivity of the material, which results in a decrease in value of $\bar{\Phi}$. ($h = 2 \mu\text{m}$, $a = b = 100h$, $h_f/h = 1$, UDL),	123
Figure 4.10:	Effect of flexoelectric layer thickness ratio h_f/h on the nondimensional potential $\bar{\Phi}$ of a cantilever flexoelectric plate ($h = 2 \mu\text{m}$, $a = b = 100h$). The maximum potential is obtained for $h_f/h = 1$	124
Figure 4.11:	Contour plots of nondimensional deflection \bar{w} of flexoelectric unimorph plate for various boundary conditions ($h = 2 \mu\text{m}$, $a = b = 100h$, $\Delta\phi = 100 \text{ V}$, $h_f/h = 0.5$).	126
Figure 4.12:	Deformation contour plots for one edge clamped flexoelectric plate under applied electrostatic potential.	127

Figure 4.13:	Effect of plate thickness on nondimensional deflection \bar{w} of a simply-supported flexoelectric composite plate ($h_f/h = 0.5$): (a) $h=2 \mu\text{m}$, (b) $h=80 \mu\text{m}$. A considerable difference among the results of classical theory, modified couple stress theory, and strain gradient theory is noted at micro-scale and this difference becomes negligible at macro scale.	127
Figure 4.14:	Effect of mechanical length scale parameters on nondimensional deflection $\bar{w}(a, b/2)$ for a cantilever flexoelectric micro-plate. The length scale parameter l_0 incorporates size effects more prominently as compared to l_1 and l_2 ($h = 2 \mu\text{m}$, $a = b = 100h$, $h_f/h = 0.5$).	128
Figure 4.15:	Effect of flexoelectric layer thickness ratio h_f/h on the nondimensional deflection \bar{e} of a cantilever flexoelectric plate ($h = 2 \mu\text{m}$, $a = b = 100h$). The nondimensional deflection is dependent on the choice of the substrate.	129
Figure 4.16:	Variation of transverse deflection w along the axis of a passive cantilever micro-beam. The present FEM results agree well with analytical results presented in (Kong <i>et al.</i> (2009)) ($h = 20 \mu\text{m}$, $b = 2h$, $L = 20h$, $L/R = 0$).	131
Figure 4.17:	Variation of nondimensional potential $\bar{\Phi}(\alpha_3 = h/2)$ along the span α_1 of the flexoelectric beam for the following boundary conditions: (a) Simply-supported at both ends, (b) Clamped at both ends, (c) Clamped at $\alpha_1 = 0$ and simply-supported at $\alpha_1 = L$, (d) Cantilever beam. ($h = 2 \mu\text{m}$, $b = h$, $L = 100h$, $h_f/h = 0.1$, $L/R = 0$), (UDL: Uniformly distributed load, SSL: Sinusoidal load, HSL: Hydrostatic load).	134
Figure 4.18:	Variation of nondimensional deflection w/h along the span length α_1 of simply-supported flexoelectric beam for different L/R ratios ($h = 2 \mu\text{m}$, $b = h$, $L = 100h$, $h_f/h = 0.1$). Our FEM results agree well with the analytical results.	135
Figure 4.19:	Variation of nondimensional deflection w/h along the span of the cantilever flexoelectric beam for different electromechanical loading conditions: (a) Effect of change in electrostatic potential, (b) Effect of change in transverse mechanical load ($h = 2 \mu\text{m}$, $b = h$, $L = 100h$, $h_f/h = 0.1$, $L/R = 0$).	136
Figure 5.1:	Reference configuration of the electroelastic membrane. κ_r represents reference volume and $\partial\kappa_r$ denotes surface boundary of the membrane. Ω_r represents the mid-surface of the membrane enclosed by boundary $\partial\Omega_r$	140
Figure 5.2:	Position vector \mathbf{r} and director vector \mathbf{d} on the deformed mid-surface surface Ω	141
Figure 5.3:	Cylindrical membrane in reference configuration.	146
Figure 5.4:	Axisymmetric deformation of the cylindrical membrane	151
Figure 5.5:	Schematic of a circular membrane in reference configuration.	156

Figure 5.6:	Deformed configuration if a circular membrane undergoing axisymmetric deformation.	158
Figure 5.7:	Undeformed and deformed configurations for circular electroelastic membrane.	161
Figure 5.8:	Limit point instability plot for passive circular membrane for different values nondimensional material parameter δ . The limit point instability is not observed for circular membranes with $\delta > 0.96$	162
Figure 5.9:	Deformation plots of passive circular membrane for different pressure and nondimensional material parameter δ values. Neo-Hookean material requires lesser pressure to attain same actuator displacement as compared to Mooney-Rivli material due to limit point instability.	163
Figure 5.10:	Deformation plot for electroelastic circular membrane under applied electric field and pressure ($\delta = 0.9, \Delta p^* = 1, V^* = 0.2$). The present results are verified with Edmiston and Steigmann (2011).	163
Figure 5.11:	Deformation and stretch plots for electroelastic circular membrane under applied pressure and electric field ($\delta = 0.9, \Delta p^* = 1$).	164
Figure 5.12:	Undeformed and deformed configurations, and coordinate system for the electroelastic cylindrical membrane.	165
Figure 5.13:	Deformation and stretch plots for electroelastic cylindrical membrane under applied pressure and electric field ($R_0/L = 1/15, \delta = 0.9091, \Delta p^* = 0.8$).	166
Figure 5.14:	Deformation plots for Neo-Hookean cylindrical membrane under applied pressure ($R_0/L = 1/15, \delta = 1, V^* = 0$).	166
Figure 5.15:	Deformation plots for Neo-Hookean electroelastic cylindrical membrane under applied pressure and electric load ($R_0/L = 1/15, \delta = 1, \Delta p^* = 0.844$).	167
Figure 5.16:	Limit point pressure plots for cylindrical membrane for applied electric field ($\delta = 0.9091, R_0/L = 2$). The limit point pressure decreases with application of electric load V^*	167
Figure 5.17:	Limit point instability plots for cylindrical membrane for applied electric field ($R_0/L = 2, \delta = 0.9091$). The symbol (\star) represents the limit point for each curve.	168

List of Tables

Table 3.1:	Nondimensional potential $\bar{\Phi}(0.5a, 0.5b, 0.5h)$ generated in a simply supported piezoelectric unimorph [0/PFRC] plate for different span-to-thickness ratios under uniform pressure. The results are verified with 3D FEM results and compared with HSDT. It is observed that our model is more accurate for thick plates.	51
Table 3.2:	Nondimensional potential $\bar{\Phi}(0.5a, 0.5b, 0.5h)$ for piezoelectric unimorph [0/PFRC] cylindrical shell under uniform pressure for various boundary conditions ($a/h = 10$). Note that IHSDT predicts better results than HSDT for all boundary conditions.	54
Table 3.3:	Nondimensional potential $\hat{\Phi}(0.5a, 0.5b, 0.5h)$ for piezoelectric unimorph [0/RS] plate for different span-to-thickness ratios subjected to in-plane shear load. The results are verified with 3D FEM results.	57
Table 3.4:	Electrostatic potential Φ (in Volts) flexural [0/PFRC], In-plane shear [0/RS] and transverse shear [0/PZT/0] sensors for different span to thickness ratios. For a thicker sensor ($a/h = 10$), the output of transverse shear sensor is more than the flexural sensor, and for a thin plate ($a/h = 100$), the flexural sensor generates more output than the transverse shear sensor.	65
Table 4.1:	Nondimensional deflection $\bar{w} = w_0 \left(\frac{10^4 f_2 h}{\Delta\phi_a \epsilon_1 a^2} \right)$ for different boundary conditions. ($h = 2 \mu\text{m}$, $ab = 100h$, $\Delta\phi = 100 \text{ V}$)	125
Table 4.2:	Nondimensional potential $\bar{\Phi}(L/2, h/2) = \frac{10^4 \phi c_0 \epsilon_1 b h^2}{q_0 f_2 L^2}$ for simply-supported flexoelectric beam under different loading conditions. Our FEM results are compared with analytical results. ($h = 2 \mu\text{m}$, $b = h$, $L = 100h$, $h_f/h = 0.1$, $c_0 = 1 \text{ GPa}$), (SSL: Sinusoidal load, UDL: Uniformly distributed load, HSL: Hydrostatic load).	133

List of Symbols

- $\Delta\phi$ Electrostatic potential applied across the electroelastic layer, see equation (4.167), page 124
- $\alpha_1, \alpha_2, \alpha_3$ Curvilinear coordinates, see equation (3.6), page 24
- δ Dimensionless material parameter, see equation (5.43), page 148
- δ_{il} Kronecker delta function, see equation (4.39), page 75
- ϵ_0 Electrical permittivity in free space, see equation (5.9), page 139
- ϵ_{ij} Components of dielectric permittivity matrix for piezoelectric material ($i, j = 1, 2, 3$), see equation (3.26), page 30
- μ_1, μ_2 Penalty parameters, see equation (3.37), page 33
- Ω Free energy function, see equation (4.1), page 67
- ω Work done by the externally applied force, see equation (4.1), page 67
- Φ Electrostatic potential across piezoelectric layer, see equation (3.22), page 29
- ϕ Scalar electrostatic potential, see equation (4.3), page 68
- ϕ_1, ϕ_2 Components of shear rotation, see equation (3.17), page 26
- Π Potential energy of the coupled electromechanical system, see equation (3.29), page 31
- ρ_s Surface charge density, see equation (3.31), page 31
- ρ_v Applied volumetric charge density, see equation (4.8), page 69
- S_I Strain components in Voigt notation ($I = 1, 2, 3, 4, 5, 6$), see equation (3.6), page 24

T_I	Stress components in Voigt notation ($I = 1, 2, 3, 4, 5, 6$), see equation (3.25), page 30
$\bar{\Phi}$	Nondimensional potential difference, see equation (3.71), page 49
\bar{w}	Nondimensional deflection, see equation (4.167), page 124
\mathbf{T}	Cauchy stress tensor, see equation (5.3), page 138
λ_j	Principle stretches ($(j = 1, 2, 3)$), see equation (5.44), page 148
B_{ij}	Higher-order electric displacement tensor, see equation (4.6), page 68
c	Young's modulus, see equation (4.165), page 117
c_{ijkl}	Stiffness tensor, see equation (4.29), page 73
D_i	Components of electric displacement vector ($i, j = 1, 2, 3$), see equation (3.26), page 30
e_{ijk}	Piezoelectric coupling tensor, see equation (4.29), page 73
e_{iJ}	Components of piezoelectric coupling matrix, see equation (3.26), page 30
E_i	Components of electric field vector ($i, j = 1, 2, 3$), see equation (3.25), page 30
$f(\alpha_3)$	Non-polynomial shear strain function, see equation (3.17), page 26
f_i^b	Body force vector, see equation (4.8), page 69
f_{ijkl}	Direct flexoelectric coupling tensor, see equation (4.29), page 73
G	Shear modulus, see equation (5.43), page 148
g_{ijklmn}	Higher-order stiffness tensor, see equation (4.29), page 73
G_{ijk}	Strain gradient Tensor, see equation (4.1), page 67
h	Thickness of the structure, see equation (3.18), page 26
h_{ijkl}	Converse flexoelectric coupling tensor, see equation (4.29), page 73
H_{ijk}	Higher-order stress tensor, see equation (4.6), page 68
I_1, I_2, I_3	Invariants of Cauchy deformation tensor, see equation (5.43), page 148

J	Determinant of deformation gradient tensor, see equation (5.3), page 138
k_{ijkl}	Higher-order electric permittivity tensor, see equation (4.29), page 73
K_{ij}	Electric field gradient tensor, see equation (4.1), page 67
l_0^e, l_1^e	Electric length scale parameters, see equation (4.51), page 77
l_0, l_1, l_2	Mechanical length scale Parameters, see equation (4.47), page 76
q_3	Applied transverse mechanical load, see equation (3.31), page 31
q_{1s}, q_{2s}	Applied in-plane shear loads, see equation (3.31), page 31
Q_{IJ}	Components of stiffness matrix for piezoelectric materials ($I, J = 1, 2, 3, 4, 5, 6$), see equation (3.25), page 30
R_1, R_2	Principal radii of curvature of a doubly curved shell, see equation (3.6), page 24
S_{ij}	Infinitesimal strain tensor, see equation (4.1), page 67
t_i^a	Applied traction vector, see equation (4.8), page 69
T_{ij}	Cauchy stress tensor, see equation (4.6), page 68
u_0	Mid-plane displacement along α_1 , see equation (3.17), page 26
u_i	Components of displacement vector ($i = 1, 2, 3$), see equation (3.6), page 24
U_T	Total internal energy, see equation (3.29), page 31
ν	Poisson's ratio, see equation (4.165), page 117
v_0	Mid-plane displacement along α_2 , see equation (3.17), page 26
W	External work done, see equation (3.29), page 31
w_0	Mid-plane displacement along α_3 , see equation (3.17), page 26
$\bar{\mathbf{d}}$	Global field variable vector, see equation (3.60), page 40
$\bar{\mathbf{F}}_{\mathbf{g}}$	Global force vector, see equation (3.64), page 41
$\bar{\mathbf{K}}_{\mathbf{g}}$	Global stiffness matrix, see equation (3.60), page 40

- C** Right cauchy green stress tensor, see equation (5.42), page 148
- R** Orthogonal rotational tensor, see equation (5.46), page 149
- U** Right stretch tensor, see equation (5.46), page 149
- V** Left stretch tensor, see equation (5.46), page 149
- X** Position of a point in reference configuration, see equation (5.11), page 140
- x** Position of a point in current configuration, see equation (5.39), page 147
- e_f** Electric field in free space, see equation (5.9), page 139
- F** Deformation gradient tensor, see equation (5.3), page 138
- I** Identity Tensor, see equation (5.9), page 139
- P** Piola stress tensor, see equation (5.1), page 137
- T_m** Maxwell stress tensor, see equation (5.9), page 139
- W** Free energy function, see equation (5.43), page 148

Acronyms

CBC	Charge Boundary Conditions
CBT	Classical Beam Theory
CLPT	Classical Laminated Plate Theory
CLST	Classical Laminated Shell Theory
DKT	Discrete Kirchhoff Technique
EAP	Electroactive Polymers
FE	Finite Element
FEM	Finite Element Method
FSDT	First Order Shear Deformation Theory
HPBC	Higher-order Potential Boundary Conditions
HSDT	Higher-order Shear Deformation Theory
HSL	Hydrostatic Load
HSM	Hybrid Stress Method
IHSDT	Inverse Hyperbolic Shear Deformation Theory
PBC	Potential Boundary Conditions
PFRC	Piezoelectric Fiber Reinforced Composite
ODE	Ordinary Differential Equation
SSL	Sinusoidal Load
UDL	Uniformly Distributed Load